Ground states and dynamical properties of the $S > 1/2$ quantum Heisenberg model on the 1/5-depleted square lattice

Jun-Han Huang [1], Zenan Liu,[1] Han-Qing Wu,[1,*] and Dao-Xin Yao[1,2,†]

[1]*Center for Neutron Science and Technology, State Key Laboratory of Optoelectronic Materials and Technologies, Guangdong Provincial Key Laboratory of Magnetoelectric Physics and Devices, School of Physics, Sun Yat-sen University, Guangzhou 510275, China*
[2]*International Quantum Academy, Shenzhen 518048, China*

We study the $S > 1/2$ antiferromagnetic Heisenberg model on the 1/5-depleted square lattice as a function of the ratio of the intraplaquette coupling to the interplaquette coupling. Using stochastic series expansion quantum Monte Carlo simulations, we numerically identify three quantum phases, including the dimer phase, Néel phase, and plaquette valence-bond-solid phase. We also obtain the accurate quantum critical points that belong to the $O(3)$ universality class using the large-scale finite-size scaling. Most importantly, we study the dynamic spin structure factors of different phases, which can be measured by inelastic neutron scattering experiments. The low-energy excitations can be explained as triplons in the dimer phase and plaquette valence-bond-solid phase, while in the Néel phase, the more prominent magnon mode can be found as the spin magnitude increases. Furthermore, we find a broader continuum at smaller S, which may be the dynamical signature of nearly deconfined spinon excitations.

I. INTRODUCTION

The 1/5-depleted square lattice has been found in some real materials, such as the compound CaV_4O_9 [1–5] and the iron-based superconductor $K_{0.8}Fe_{1.6}Se_2$ [6–18]. To understand the magnetic properties of these materials, we can study the Heisenberg model with competing intraplaquette, interplaquette, and other range exchange interactions. Among them, the competition of two unfrustrated intraplaquette and interplaquette exchange interactions can induce quantum phase transitions between the Néel-ordered phase and two valence-bond-solid phases [see Fig. 1(a)], which can be handled by large-scale quantum Monte Carlo (QMC) simulation. Despite the well-studied $S = 1/2$ case, it is still worth accurately estimating the quantum critical points and studying its dynamical properties of this unfrustrated model in the higher-spin case. It is worth mentioning that the square-octagon lattice is topologically equivalent to the 1/5-depleted square lattice. The former lattice can be realized in a carbon-based material that can host superconductivity with doping [19–21].

Here, we briefly review some previous studies of the $S = 1/2$ Heisenberg model on the 1/5-depleted square lattice [4,22–29]. When the ratio of the intraplaquette coupling J to the interplaquette coupling J' tends to zero, the ground state of this model belongs to a dimer phase and it can be effectively projected into a total $S = 2$ Affleck-Kennedy-Lieb-Tasaki (AKLT) state on the square lattice [30], whereas the system forms a plaquette valence-bond-solid (PVBS) phase in the limit $J/J' \to \infty$. In between two gapped VBS

phases, there is an intermediate Néel ordered phase, and two quantum critical points were estimated to be $J/J' = 0.603520(10)$ and $J/J' = 1.064382(13)$, respectively [30]. Thus, the slightly stronger intraplaquette coupling or the frustrating next-nearest-neighbor interaction gives rise to the gapped PVBS phase, which has been used to explain the spin gap observed in the compound CaV_4O_9 [3–5].

For a higher-spin case, the spin-S AKLT state can be realized when the lattice coordination number z and the spin quantum number S satisfy the relation $z = 2S/n$, where n is a positive integer number [31–33]. Importantly, the AKLT states on most two-dimensional Archimedean lattices are universal resources for measurement-based quantum computation [34–42]. The $S = 3/2$ AKLT model on the honeycomb is a weak symmetry-protected topological (SPT) phase that is protected by translational symmetry rather than the on-site symmetry [43,44], and it can be probed effectively by the strange correlator [45–47]. The $S = 3/2$ model on a 1/5-depleted square lattice also satisfies the relation $z = 2S/n$ and can form the AKLT phase shown in Fig. 1(b), in which each spin-3/2 physical particle can divide into three virtual spin-1/2 degrees of freedom and each two neighboring virtual spin-1/2 particles belonging to different physical particles can form a singlet. However, previous study has suggested that the AKLT model and the Heisenberg model may be not in the same phase on a trivalent lattice, unlike the one-dimensional chain [32,48–51]. The $S = 3/2$ AKLT model on the 1/5-depleted square lattice that contains the biquadratic and bicubic terms is left for future study. In this paper, we mainly study the $S > 1/2$ antiferromagnetic Heisenberg model on the 1/5-depleted square lattice with only nearest-neighbor interactions by using large-scale QMC simulations. We study the evolutions of phase boundaries and
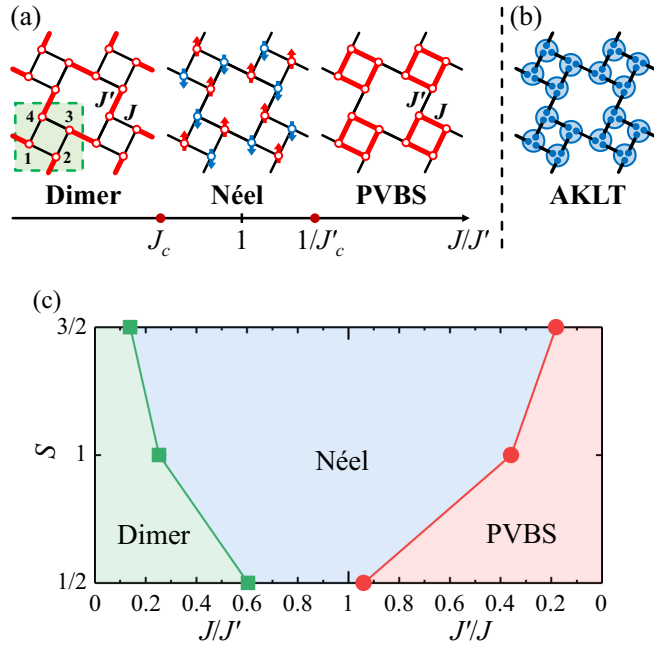
*wuhanq3@mail.sysu.edu.cn
†yaodaox@mail.sysu.edu.cn

FIG. 1. (a) The schematic phase diagram of the antiferromagnetic Heisenberg model on the 1/5-depleted square lattice, including two VBS phases and one Néel phase in between. J and J' are the intraplaquette and interplaquette interactions, respectively. The green dashed square shows a unit cell with the sublattice labels $\alpha = 1, 2, 3, 4$. (b) Illustration of the spin-3/2 AKLT state on the 1/5-depleted square lattice. Each spin-3/2 physical particle (blue large circles) can be regarded as the symmetric subspace of three virtual spin-1/2 particles (blue small circles). (c) The phase boundaries of the Heisenberg model with different spin magnitudes $S = 1/2, 1, 3/2$. We set $J = 1$ when $J > J'$, and set $J' = 1$ when $J < J'$ in turn.

dynamical properties as the spin magnitude S increases. Our numerical results can help to understand the magnetic properties of Mott insulators with multiorbitals on the 1/5-depleted square lattice or its topologically equivalent square-octagon lattice.

The rest of the paper is organized as follows. In Sec. II, we introduce the Hamiltonian and the QMC methods for the higher-spin case. In Sec. III, we study the phase boundaries based on the finite-size scaling hypothesis at criticality (see Fig. 1) and we also study the dynamic spin structure factor of different phases by stochastic analytic continuation of QMC data. Section IV gives our final conclusion.

II. MODEL AND METHODS

We study the $S > 1/2$ antiferromagnetic Heisenberg model on a 1/5-depleted square lattice, which is topologically equivalent to a square-octagon lattice. The Hamiltonian is expressed as

$$H = J \sum_{\langle ij \rangle} \mathbf{S}_i \cdot \mathbf{S}_j + J' \sum_{\langle ij \rangle'} \mathbf{S}_i \cdot \mathbf{S}_j, \qquad (1)$$

where $\mathbf{S}_i$ denotes the spin-S operator on each site i, $\langle ij \rangle$ denotes nearest-neighbor sites on the intraplaquette bonds, and $\langle ij \rangle'$ denotes the interplaquette bonds. $J, J' > 0$ are the intraplaquette and interplaquette antiferromagnetic couplings, respectively. For simplicity, we set $J' = 1$ for $J \leqslant J'$, and $J = 1$ for $J > J'$ in the whole paper. Thus, the two potential quantum critical points can be expressed as J_c ($J' = 1$) and J'_c ($J = 1$), respectively.

To obtain the phase boundaries of the Heisenberg model on the 1/5-depleted square lattice, we employ sign-free QMC simulations based on the stochastic series expansion, which has been described in detail in Refs. [52–55]. Here, we briefly summarize two important update schemes used in the higher-spin case, comparing with the standard spin-1/2 one.

The first one is diagonal updates. Because of the nonuniform coupling strengths on the interplaquette bonds and intraplaquette bonds, we consider the following acceptance probabilities to satisfy detailed balance:

$$P([0,0]_p \to [1,b]_p) = \min\left[\frac{J_b N_b \beta \langle \alpha(p)|H_{1,b}|\alpha(p)\rangle}{L_n - n}, 1\right],$$

$$P([1,b]_p \to [0,0]_p) = \min\left[\frac{L_n - n + 1}{J_b N_b \beta \langle \alpha(p)|H_{1,b}|\alpha(p)\rangle}, 1\right]. \qquad (2)$$

Here L_n is the cutoff of the operator string and n is the number of the nonunit operators. J_b represents J and J' on the intraplaquette and interplaquette bonds, respectively. More detailed explanations can be found in Ref. [52].

The second one is operator-loop updates. For the higher-spin case, even without external magnetic field and anisotropy, there are four possible paths through the vertices, including bounce, continue-straight, switch-and-reverse, and switch-and-continue processes [54]. First, the operator loop starts at a random position on one of the vertices and the spin state on this position is changed to one of the other $2S$ possible states. Next, according to the detailed balance condition, the paths are chosen with a probability proportional to the vertex weight. This procedure is repeated until the loop reaches the initial position, meanwhile with a same spin state.

III. NUMERICAL RESULTS

We mainly explore the $S > 1/2$ antiferromagnetic Heisenberg model on a 1/5-depleted square lattice with periodic boundary condition and the inverse temperature $\beta = 1/T = \sqrt{N}$ (i.e., $\beta = 2L$) unless specifically mentioned. Here, L represents the linear number of the unit cells as shown in Fig. 1(a).

A. The spin-3/2 case

First, we study the phase boundaries of the $S = 3/2$ Heisenberg model on the 1/5-depleted square lattice. Two dimensionless quantities, the L-normalized uniform magnetic susceptibility χL and the spin stiffness $\rho_s L$ are used to detect the quantum critical points. The uniform magnetic susceptibility and the spin stiffness are expected to scale as $\chi \sim L^{z-d}$ and $\rho_s \sim L^{2-z-d}$ at the quantum critical points. Here, $d = 2$ is the spatial dimension and $z = 1$ is the dynamic critical exponent due to the three-dimensional $O(3)$ universality class in this
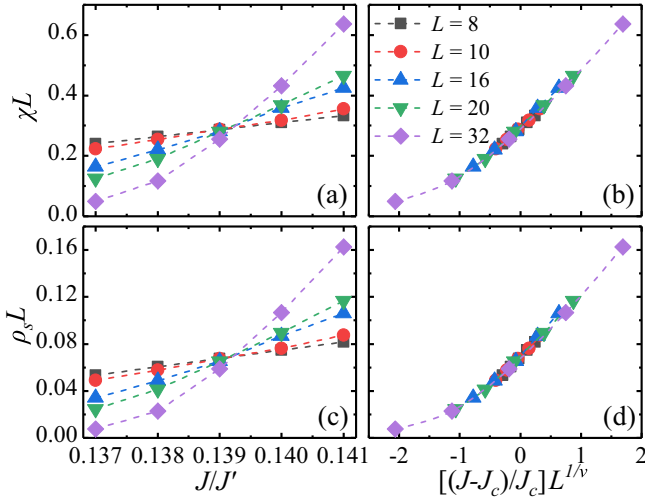
FIG. 2. (a), (b) The uniform magnetic susceptibility multiplied by L and (c), (d) the spin stiffness multiplied by L of the $S = 3/2$ antiferromagnetic Heisenberg model on the 1/5-depleted square lattice with $L = 8, 10, 16, 20, 32$ near the quantum critical point J_c. The results are obtained from QMC simulations. Data collapses are achieved for a fixed standard $O(3)$ value $1/\nu = 1.406$ and $J_c = 0.1392(2)$.
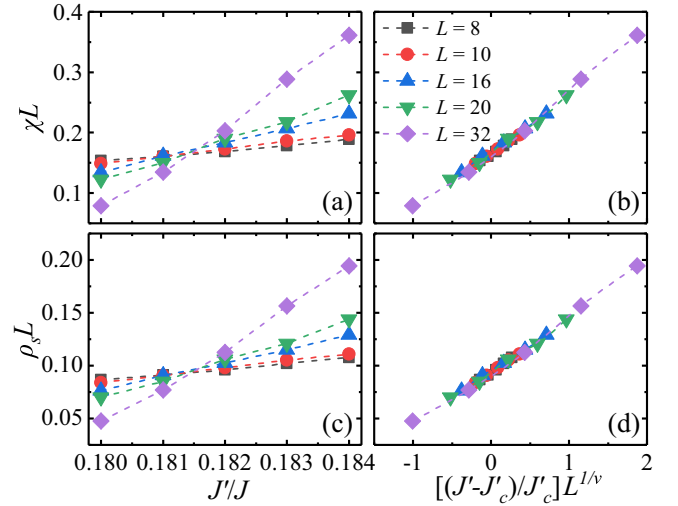

FIG. 3. (a), (b) The uniform magnetic susceptibility multiplied by L and (c), (d) the spin stiffness multiplied by L of the $S = 3/2$ antiferromagnetic Heisenberg model on the 1/5-depleted square lattice with $L = 8, 10, 16, 20, 32$ near the quantum critical point J'_c. The results are obtained from QMC simulations. Data collapses are achieved for a fixed standard $O(3)$ value $1/\nu = 1.406$ and $J'_c = 0.1814(4)$.

model [56]. Thus, the two dimensionless quantities χL and $\rho_s L$ are expected to be fixed values for different linear lattice sizes L at the quantum critical points.

The uniform magnetic susceptibility χ is defined as

$$\chi = \frac{\beta}{N} \left\langle \left(\sum_{i=1}^{N} S_i^z \right)^2 \right\rangle, \tag{3}$$

and the x direction of spin stiffness ρ_s^x can be obtained from

$$\rho_s^x = \frac{3}{2\beta N} \langle (N_x^+ - N_x^-)^2 \rangle, \tag{4}$$

where N_x^+ and N_x^- are the total number of off-diagonal operators transporting spin along the positive and negative x direction, respectively. The derivations of Eqs. (3) and (4) are expounded in Ref. [52]. The spin stiffness ρ_s^y in the y direction has the same definition as Eq. (4). In practice, we extract spin stiffness from $\rho_s = (\rho_s^x + \rho_s^y)/2$ on the topologically equivalent square-octagon lattice with spatial isotropy.

To obtain the quantum critical points, we calculate the dimensionless quantities χL and $\rho_s L$ with different linear sizes $L = 8, 10, 16, 20, 32$. As shown in Figs. 2(a) and 2(c), the uniform magnetic susceptibility χL and the spin stiffness $\rho_s L$ measured on different L both roughly cross each other at the first critical point J_c, which confirms that a continuous quantum phase transition occurs between a dimer phase and a Néel phase [57]. When the coupling ratio $J/J' < J_c$, the uniform magnetic susceptibility χL gradually goes to zero as the linear size L is increased and the gapped dimer phase emerges as expected.

According to the finite-size scaling hypothesis at criticality, the dimensionless quantities satisfy the following form [52,58]:

$$Q(t, L) \sim f_Q(tL^{1/\nu}), \tag{5}$$

where $t = (J - J_c)/J_c$ for $J \leqslant J'$ is the reduced coupling and ν is the correlation length exponent. In the finite-size scaling analysis, we try to fix the correlation length exponent ν at the known most accurate $O(3)$ value $1/\nu = 1.406$ via classical three-dimensional Heisenberg simulations [59–62]. Then we can proceed to perform data collapses in order to get a better estimate of the critical point J_c based on Eq. (5). It is worth noting that the lack of a certain local symmetry can bring about corrections to the $O(3)$ universality class, e.g., in the staggered dimerized model [62–64].

As shown in Figs. 2(b) and 2(d), we present the results of the dimensionless quantities χL and $\rho_s L$ versus the reduced quantity $tL^{1/\nu}$. The good data collapses of χL and $\rho_s L$ are achieved at $J_c = 0.1392(2)$ when we set $J' = 1$. Therefore, with the knowledge of the three-dimensional $O(3)$ universality class as expected, we get the accurate estimation of the first quantum critical point that is $J_c = 0.1392(2)$.

Next, we focus on the second quantum critical point in the phase diagram of the $S = 3/2$ Heisenberg model on the 1/5-depleted square lattice. The uniform magnetic susceptibility χL and the spin stiffness $\rho_s L$ with different L cross each other again at the other critical point J'_c (see Fig. 3). Here we would like to emphasize that the second quantum critical point occurs at $J > J'$ instead of $J \leqslant J'$. Moreover, a good data collapse of χL and $\rho_s L$ with the accurate value $1/\nu = 1.406$ for the $O(3)$ universality class are obtained based on finite-size scaling as shown in Figs. 3(b) and 3(d). The quantum critical point of this continuous phase transition is estimated to be $J'_c = 0.1814(4)$ when we set $J = 1$. And the disordered and gapped PVBS phase can be found when the ratio of the intraplaquette coupling J' to the interplaquette coupling J is less than 0.1814(4).

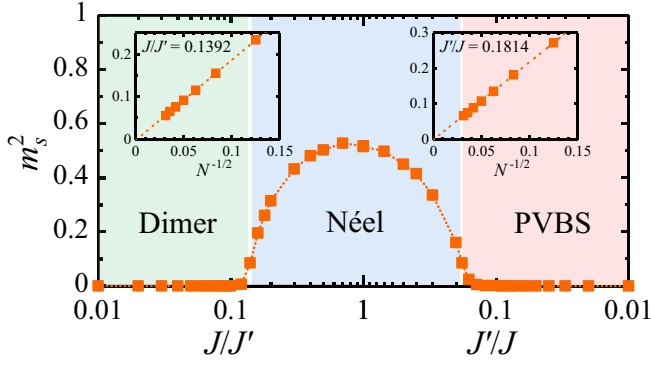Therefore, two quantum critical points of the $S = 3/2$ Heisenberg model on the 1/5-depleted square lattice are

FIG. 4. The phase diagram of the $S = 3/2$ antiferromagnetic Heisenberg model on the 1/5-depleted square lattice consists of the dimer phase, Néel phase, and PVBS phase. The squared staggered magnetization m_s^2 is obtained from QMC simulations on this lattice with $L = 8$ in the whole phase regions. The insets show the finite-size dependence of m_s^2 with linear sizes $L = 4, 6, 8, 10, 12, 14, 16$ near the quantum critical points $J/J' = 0.1392$ (left) and $J'/J = 0.1814$ (right), respectively. The error bars are smaller than the symbols.

obtained accurately to be $J_c = 0.1392(2)$ and $J'_c = 0.1814(4)$ using finite-size scaling. In Fig. 1(c), we show the phase diagram of this model versus the coupling ratios J/J' for $J \leqslant J'$ and J'/J for $J > J'$, respectively. The dimer phase and the PVBS phase represent the spin singlets formed on the interplaquette bonds and plaquettes, respectively [65]. What's more, in the dimer phase, the spin-3/2 singlets are expected on the dimer bonds, and an effective gapless spin-3/2 chain is speculated to be formed by the dangling spins on the open edge similar to the spin-1/2 case [30,66]. In addition, the dimer order and plaquette order can be revealed from the critical behavior of the spin correlations on the different bonds at the quantum phase transition, which are discussed in Appendix A in more detail.

With the coordination number $z = 3$ of the 1/5-depleted square lattice, an AKLT state can be formed in the spin-3/2 case. However, due to the nature of the two-dimensional bipartite lattice, the ground state of the pure Heisenberg model without biquadratic and bicubic terms is more likely to be a Néel phase for arbitrary S. Next, we numerically calculate the spin correlations and get the extrapolated magnetic order in the intermediate Néel phase. We also have numerically confirmed that other magnetic orders, such as block antiferromagnetic orders, are not the ground state whatever the spin magnitude is. To detect the Néel order, we define the squared staggered magnetization as

$$m_s^2 = \frac{1}{N^2} \left\langle \left(\sum_{i=1}^N (-1)^i S_i^z \right)^2 \right\rangle, \quad (6)$$

where $(-1)^i = \pm 1$ is the staggered phase factor according to the Néel-type spin configuration as illustrated in Fig. 1(a). The finite-size scaling of the staggered magnetization is expected to be of order $O(N^{-1/2})$ [67,68].

In Fig. 4, the squared staggered magnetization m_s^2 in the thermodynamic limit is shown versus the coupling ratios J/J' for $J \leqslant J'$ and J'/J for $J \geqslant J'$, respectively. The squared stag-

gered magnetization gradually decreases to zero as expected in the disordered dimer phase and the PVBS phase. The insets of Fig. 4 further show the finite-size dependence of m_s^2 as a function of $N^{-1/2}$, in which total sites like $N = 64, 144, 256, 400, 576, 784, 1024$ (where $N = 4L^2$) are used to do the extrapolations. The squared staggered magnetization m_s^2 is extrapolated to zero in the thermodynamic limit at these two quantum critical points. However, the Néel order parameter m_s^2 in the intermediate phase as shown in Fig. 4 is enhanced compared to the spin-1/2 case.

In conclusion, we have got the phase diagram of the $S = 3/2$ antiferromagnetic Heisenberg model on the 1/5-depleted square lattice, including the dimer phase,
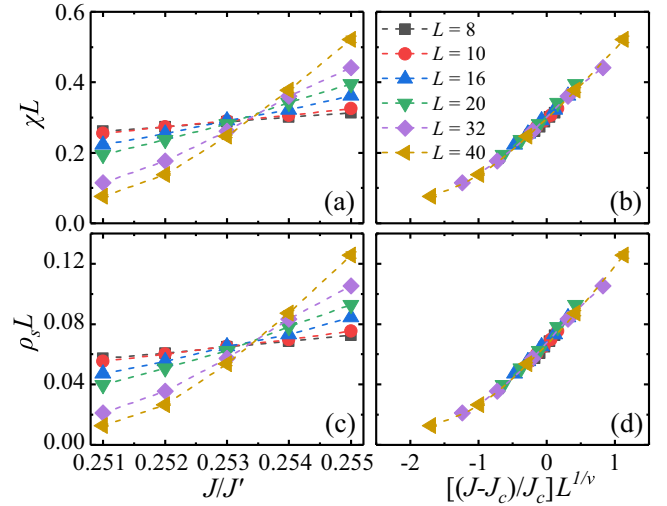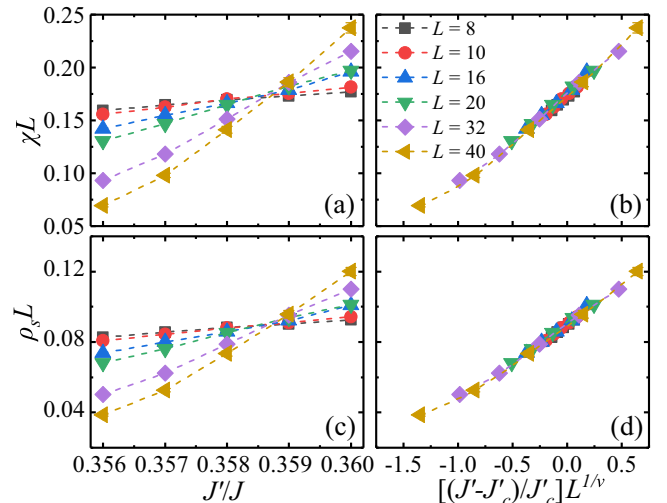

FIG. 5. (a), (b) The uniform magnetic susceptibility multiplied by L and (c), (d) the spin stiffness multiplied by L of the $S = 1$ antiferromagnetic Heisenberg model on the 1/5-depleted square lattice near the quantum critical point J_c. Data collapses are achieved for a fixed standard $O(3)$ value $1/\nu = 1.406$ and $J_c = 0.2534(4)$.

FIG. 6. (a), (b) The uniform magnetic susceptibility multiplied by L and (c), (d) the spin stiffness multiplied by L of the $S = 1$ antiferromagnetic Heisenberg model on the 1/5-depleted square lattice near the quantum critical point J'_c. Data collapses are achieved for a known standard $O(3)$ value $1/\nu = 1.406$ and $J'_c = 0.3587(4)$.

TABLE I. The estimated results of the quantum critical points on the 1/5-depleted square lattice for different spins. The phase boundaries for the spin-1/2 case are quoted from Ref. [30].

Spin S	J_c ($J' = 1$)	J'_c ($J = 1$)
1/2	0.603520(10)	0.939512(12)
1	0.2534(4)	0.3587(4)
3/2	0.1392(2)	0.1814(4)

the Néel phase, and the PVBS phase with the quantum critical points $J_c = 0.1392(2)$ and $J'_c = 0.1814(4)$. These two quantum phase transitions between the two valence-bond-solid phases and the symmetry-broken phase with long-range Néel order both belong to the three-dimensional $O(3)$ universality class by mapping it to a nonlinear σ model [69,70]. Our numerical results confirm the standard $O(3)$ critical exponent based on the convincing data collapses for large-scale finite-size scaling. We also show the magnetization of the Néel phase in the thermodynamic limit.

B. The spin-1 case

In this section, we explore the ground-state properties of the $S = 1$ antiferromagnetic Heisenberg model on the 1/5-depleted square lattice to seek rule without further calculations on other higher-spin case. Similar to the spin-3/2 case, we can get the phase boundaries with high accuracy by using large-scale finite-size scaling.

To get the quantum critical points, we also extract the two dimensionless quantities, the L-normalized uniform magnetic susceptibility χL and the spin stiffness $\rho_s L$ defined in Eqs. (3) and (4). Figures 5(a) and 5(c) show the results of χL and $\rho_s L$ with various linear sizes $L = 8, 10, 16, 20, 32, 40$ near the quantum critical point J_c between the dimer phase and the Néel phase. Figures 5(b) and 5(d) show a good data collapse with a fixed standard $O(3)$ value $1/\nu = 1.406$ and an accu-
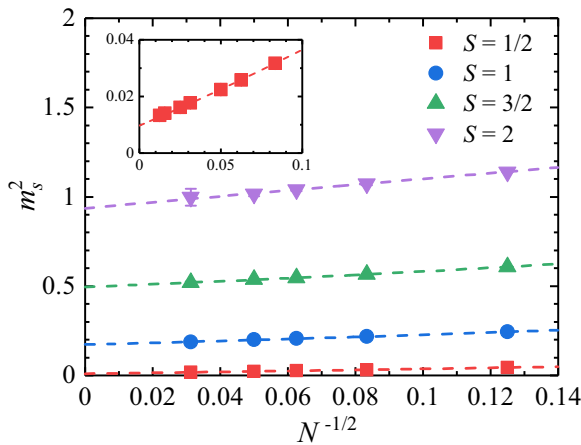

FIG. 7. The squared staggered magnetization m_s^2 of the antiferromagnetic Heisenberg model on the 1/5-depleted square lattice as a function of $N^{-1/2}$ (where $N = 4L^2$) at $J/J' = 1$ for different spins $S = 1/2, 1, 3/2, 2$. The dashed curves are the second-order polynomial fits. The inset shows more details about the finite-size extrapolation for the spin-1/2 case.
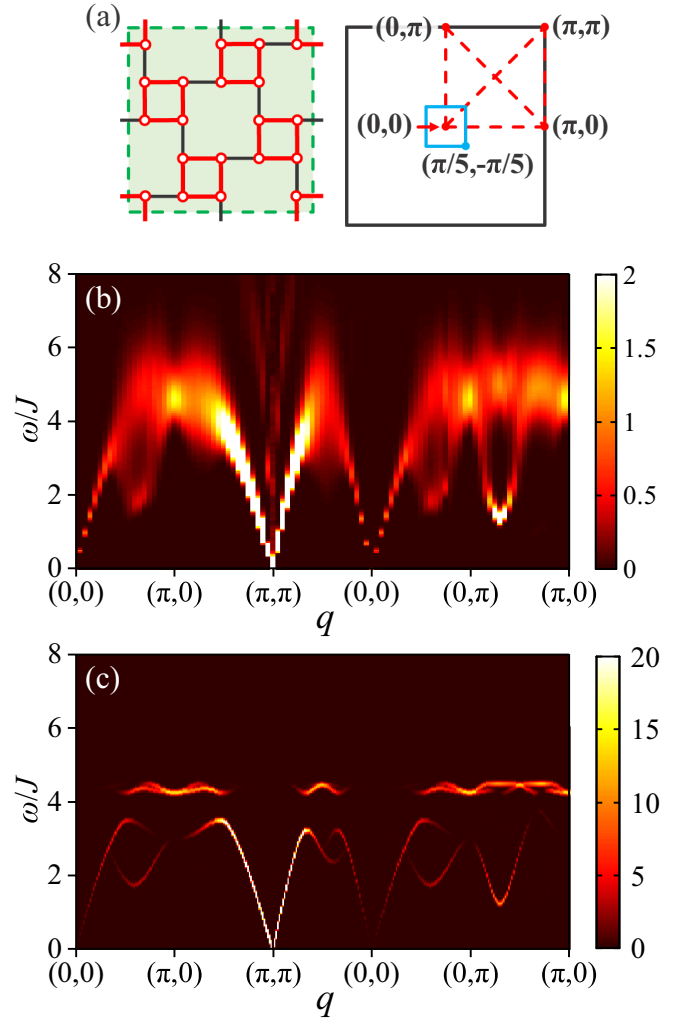

FIG. 8. (a) Left panel: The 20-site supercell (green dashed square) on the 1/5-depleted square lattice. Right panel: The folded Brillouin zone (blue small solid square) and the wave vector path (red dashed lines) in the extended Brillouin zone. (b) and (c) show the dynamic spin structure factor $S^{zz}(\boldsymbol{q}, \omega)$ of the $S = 3/2$ antiferromagnetic Heisenberg model on the 1/5-depleted square lattice at $J/J' = 1$ which is in the Néel phase. (b) is obtained from QMC simulations and stochastic analytic continuation with linear system size $M = 8$ of supercell and $\beta = 40$. (c) is obtained from linear spin wave theory.

rate estimate $J_c = 0.2534(4)$ according to finite-size scaling hypothesis at criticality. Therefore, the quantum phase transition from the dimer phase to the Néel phase is a continuous transition with the critical point $J_c = 0.2534(4)$.

As seen in Figs. 6(a) and 6(c), the uniform magnetic susceptibility χL and the spin stiffness $\rho_s L$ with different linear sizes L both also cross each other at the quantum critical point J'_c between the Néel phase and the PVBS phase in the $S = 1$ case. Similarly, we fix the correlation length exponent at the standard $O(3)$ value $1/\nu = 1.406$ and perform finite-size data collapse fits to find a precise estimate of J'_c as shown in Figs. 6(b) and 6(d). The quantum critical point between the Néel phase and the PVBS phase is estimated to be $J'_c = 0.3587(4)$. We summarize the accurate estimations of
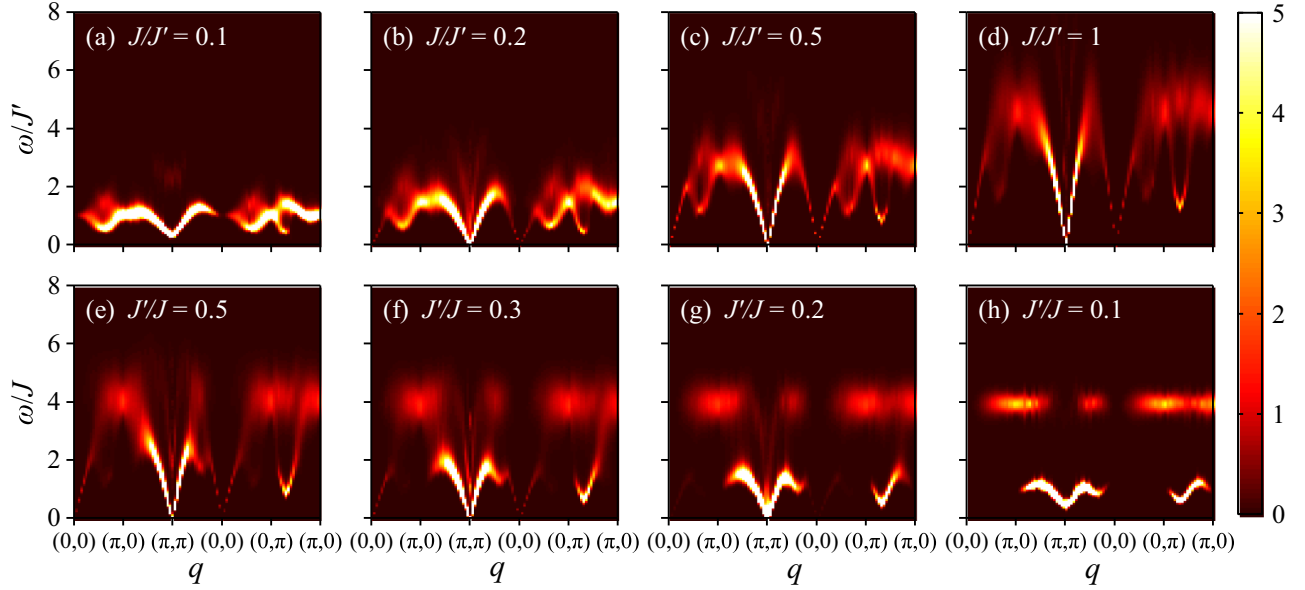
FIG. 9. The dynamic spin structure factor $S^{zz}(\boldsymbol{q}, \omega)$ obtained from QMC simulations and stochastic analytic continuation for the $S = 3/2$ antiferromagnetic Heisenberg model on the 1/5-depleted square lattice with linear system size $M = 8$ of supercell and $\beta = 40$. Here (a) is in the dimer phase, (b)–(g) are in the Néel phase and (h) is in the PVBS phase.

the quantum critical points for $S \geqslant 1/2$, which are listed in Table I.

Additionally, to verify the suppression of quantum fluctuation when S gets larger and goes to the classical Heisenberg limit, we calculate the squared staggered magnetization m_s^2 defined in Eq. (6) with different S. Figure 7 shows the finite-size extrapolations of m_s^2 versus $N^{-1/2}$ on the 1/5-depleted square lattice with different system sizes $N = 64, 144, 256, 400, 1024$ at $J/J' = 1$. As we expect, the squared staggered magnetization for different spins can be extrapolated to nonzero values in the thermodynamic limit by using the second-order polynomial fits. The finite-size scaling results of the squared z-component staggered magnetization are $m_s^2 = 0.0097(3), 0.172(6), 0.495(3), 0.935(16)$ for the spin magnitudes $S = 1/2, 1, 3/2, 2$, respectively. Here, we only consider the z component of the squared staggered magnetization, so the estimates are one third of the square of total staggered magnetization. For the spin-1/2 case, the long-range antiferromagnetic order is relatively small due to the quantum fluctuation and depleted characteristics, whereas the antiferromagnetic order shows a considerable increase toward the classical limit as S gets larger.

To conclude, we get the accurate critical points in the phase diagrams of the Heisenberg model on the 1/5-depleted square lattice for various spin magnitudes, which are summarized in Table I. The whole phase diagrams versus the coupling ratios for different spins $S = 1/2, 1, 3/2$ are shown in Fig. 1(c). A higher proportion of the intermediate Néel phase can be found on the lattice with higher spins, which means that the disordered dimer and PVBS phases originate from the quantum nature of magnetic systems.

C. Magnetic excitations

Next, we study the spin excitations of the spin-3/2 Heisenberg antiferromagnet on the 1/5-depleted square lattice.

The longitudinal dynamic spin structure factor $S^{zz}(\boldsymbol{q}, \omega)$ is obtained from the QMC simulations combined with stochastic analytic continuation along the path $(0, 0) \rightarrow (\pi, 0) \rightarrow (\pi, \pi) \rightarrow (0, 0) \rightarrow (0, \pi) \rightarrow (\pi, 0)$ of the extended Brillouin zone. To make more momentum points fall into that path in the finite-size lattice, we choose the lattices to be the multiples of the supercell shown in Fig. 8(a) [71].

In Fig. 8(b), we show the dynamic spin structure factor $S^{zz}(\boldsymbol{q}, \omega)$ of the $S = 3/2$ antiferromagnetic Heisenberg model on the 1/5-depleted square lattice with linear system size $M = 8$ of supercell [illustrated in the left panel of Fig. 8(a)] and $\beta = 40$ at the coupling ratio $J/J' = 1$, which belongs to the Néel phase. And the total lattice size is equal to $N = 20M^2$. From the excitation spectra, the gapless Goldstone mode can be found at the wave vector $\boldsymbol{q} = (\pi, \pi)$ as we expect. And the spectral weight of the gapless magnon mode nearly vanishes at $\boldsymbol{q} = (0, 0)$ due to the conservation of S^z [72,73]. Moreover, a unique magnon dispersion occurs between the wave vectors $\boldsymbol{q} = (0, \pi)$ and $(\pi, 0)$ because of the presence of a magnon pole around $\boldsymbol{q} \approx (\pi/5, 3\pi/5)$, owing to the depleted characteristic of the lattice and the Brillouin zone folding.

To further understand the spin excitations, we show the results of the dynamic spin structure factor $S^{zz}(\boldsymbol{q}, \omega)$ obtained by linear spin-wave theory as can be seen in Fig. 8(c). A Holstein-Primakoff transformation is performed to bosonize the Hamiltonian, in which the spin operators can be replaced by the boson creation and annihilation operators [74]:

$$\begin{aligned} S_i^z &= S - a_i^\dagger a_i, \quad S_i^+ \approx \sqrt{2S} a_i, \quad S_i^- \approx \sqrt{2S} a_i^\dagger, \\ S_j^z &= b_j^\dagger b_j - S, \quad S_j^+ \approx \sqrt{2S} b_j^\dagger, \quad S_j^- \approx \sqrt{2S} b_j, \end{aligned} \tag{7}$$

where $a_i^\dagger, a_i$ ($b_j^\dagger, b_j$) are for up (down) spins as illustrated in Fig. 1(a). Then the spin-wave dispersions and dynamic spin structure factor $S^{zz}(\boldsymbol{q}, \omega)$ can be calculated after diagonaliz-
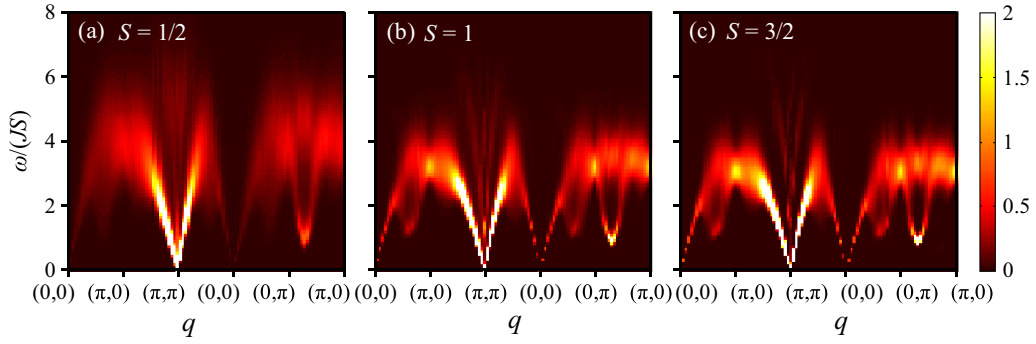
FIG. 10. The dynamic spin structure factor $S^{zz}(\boldsymbol{q}, \omega)$ of the antiferromagnetic Heisenberg model on the 1/5-depleted square lattice with linear system size $M = 8$ of supercell and $\beta = 40$ at $J/J' = 1$ for different spins $S = 1/2, 1, 3/2$. The results are obtained from QMC simulations and stochastic analytic continuation.

ing the Hamiltonian. As shown in Fig. 8(c), the spin wave can nicely capture the low-energy excitation spectra obtained from the QMC simulations. However, there are nearly flat bands in the high energy separating from the low-energy branches in the spin-wave dispersions, which is different from the high-energy broad spectrum of the QMC results (see Fig. 8). Here, we provide some potential reasons to account for the high-energy part. First, the stochastic analytic continuation numerical methods have not yet distinguished the multimagnon continua and the single-magnon quite well in a small range of frequencies [75]. Second, the high-energy continua may be contributed by magnons with strong interactions and even nearly deconfined spinons, which cannot be simply captured by the linear spin-wave theory [76]. And the presence or absence of the nearly deconfined excitations around $\boldsymbol{q} = (\pi, 0)$ and $(0, \pi)$ need to be further confirmed.

When the coupling ratio J/J' keep decreasing toward the quantum critical point $J_c = 0.1392(2)$, the excitation spectra are gradually pushed to lower energy and tend to be gapped at the wave vectors $\boldsymbol{q} = (0, 0)$ and (π, π) as shown in Figs. 9(b)–9(d). In the dimer phase, we choose a representative point $J/J' = 0.1$ ($J' = 1$) to study the dynamical properties. In Fig. 9(a), we show the dynamic spin structure factor $S^{zz}(\boldsymbol{q}, \omega)$ at $J/J' = 0.1$ using the QMC simulations and stochastic analytic continuation. The excitation spectrum is gapped as expected. The spin singlets can form on the dimer bonds. And a dimer singlet can be excited to a triplet that can move in the whole lattice, which is a well-known triplon excitation [77]. Further decreasing J/J' to the isolated dimer limit, a nearly flat band can be observed in the spectrum, which is consistent with the exact diagonalization results shown in Appendix B. In Figs. 9(e)–9(g), we also show the evolution of the excitation spectra when J'/J decreases (i.e., J/J' increases) toward the quantum critical point $J'_c = 0.1814(4)$. An observable separation process can be found between the low-energy magnon mode and the high-energy continuum. It is worth mentioning that the separation does not occur exactly at the critical point. More discussions in other spin-S system can be found in Appendix C. Similarly, we choose the coupling ratio $J'/J = 0.1$ ($J = 1$) for the PVBS phase. In Fig. 9(b), a fully gapped spectrum can also be found, and a prominent triplon mode appears around $\omega = 1.0$. In the high-energy part, there is another excitation separating from the low-energy triplon mode in the PVBS phase [71], which can be captured by the energy spectrum of the isolated plaquette.

In addition, we also extract the excitation spectra of the spin-1/2 and spin-1 cases, aiming to compare the similarities and differences between the spin-3/2 and lower-spin case. As shown in Fig. 10, the dynamic spin structure factor $S^{zz}(\boldsymbol{q}, \omega)$ at $J/J' = 1$ are shown for different spins $S = 1/2, 1, 3/2$, which all belong to the Néel phase [see Fig. 1(c)]. The overall shapes of the spin-1/2 and spin-1 excitation spectra are similar to the spin-3/2 case due to the existence of the gapless Goldstone mode in the Néel phase. The more detailed results of the dynamic spin structure factor $S^{zz}(\boldsymbol{q}, \omega)$ at the wave vector $\boldsymbol{q} = (\pi, 0)$ are shown in Fig. 11. A broader high-energy continuum can be found in the excitation spectra of the lower-spin case, especially for $S = 1/2$, which may indicate the presence of the nearly deconfined spinons [78]. However, for the higher-spin case, the broad continuum disappears, which may be due to the confinement of spinons in the classical limit $S \to \infty$.

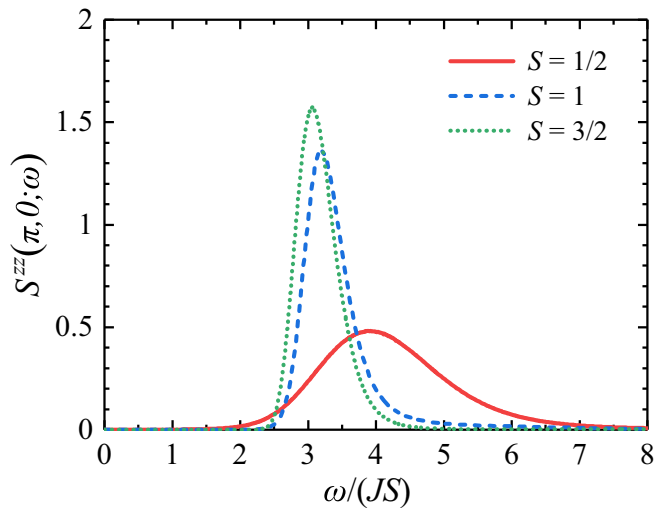FIG. 11. The dynamic spin structure factor $S^{zz}(\boldsymbol{q}, \omega)$ of the uniform antiferromagnetic Heisenberg model on the 1/5-depleted square lattice with $M = 8$ and $\beta = 40$ at the wave vector $\boldsymbol{q} = (\pi, 0)$ for different spins $S = 1/2, 1, 3/2$.

IV. CONCLUSION

In this paper, we have revealed the phase diagram of the spin $S > 1/2$ antiferromagnetic Heisenberg model on the

1/5-depleted square lattice. By using the extensive finite-size scaling of the QMC results, we obtain the accurate quantum critical points and numerically verify that the continuous quantum phase transitions belong to the three-dimensional $O(3)$ universality class with standard critical exponents.

To generalize to other higher-spin cases, we have representatively studied the ground-state properties of 1/5-depleted square-lattice Heisenberg model for the spin-1 and spin-3/2 case. According to the QMC results, when the spin magnitude increases, the magnetic order enhances, and the region of Néel phase extends to a larger area. Thus, in the higher spin case, very weak interactions between the plaquettes (or dimers) can give rise to the Néel phase. In other words, quantum fluctuation becomes very weak to suppress the long-range antiferromagnetic order as the spin magnitude increases.

Moreover, we have studied the dynamical properties of the $S = 3/2$ Heisenberg model versus the coupling ratio on the 1/5-depleted square lattice. The dynamic spin structure factor $S^{zz}(\boldsymbol{q}, \omega)$ is well extracted by using stochastic analytic continuation of the imaginary-time correlation function obtained from the QMC simulations. In the dimer phase and the PVBS phase, the low-energy excitations are numerically verified as the gapped triplons. In the Néel phase, there are well-defined gapless Goldstone modes (magnons) at the wave vectors $\boldsymbol{q} = (\pi, \pi)$ and $(0,0)$, which is consistent with the linear spin wave theory, and the depleted characteristic of the lattice and the Brillouin zone folding give rise to a magnon pole around $\boldsymbol{q} \approx (\pi/5, 3\pi/5)$. What's more, the evolution of the separation between the low-energy and high-energy spectra can be well studied owing to the two triplet excitations in the isolated PVBS limit. Finally, we have also calculated the dynamic spin structure factor $S^{zz}(\boldsymbol{q}, \omega)$ for the spin-1/2 and spin-1 cases. The excitation spectra of the lower-spin case show a broader continuum, especially at $(\pi, 0)$ and $(0, \pi)$, suggesting that the nearly deconfined spinons may exist.

The spin-S Heisenberg model on the 1/5-depleted square lattice can be simulated with ultracold atoms in optical lattices in the future or be synthesized in more Mott insulators with multiorbitals. Our numerical results can provide guidance for realizing different phases in this model, and the excitation spectra with different spin magnitudes provide a playground for studying the gapped triplons, magnons, and possible nearly deconfined spinons, which can be identified in inelastic neutron scattering and related experiments. Moreover, adding the biquadratic and bicubic interactions in the $S = 3/2$ case can induce an AKLT phase and some other phases, which is still worthy to study by the density matrix renormalization group and tensor network in the future.

APPENDIX A: SPIN CORRELATIONS ON THE DIMER AND PLAQUETTE BONDS

In this Appendix, we discuss the dimer order and the plaquette order of the spin-3/2 antiferromagnetic Heisenberg model on the 1/5-depleted square lattice. To detect the dimer and the plaquette orders in different phases, we can use the spin correlations of interplaquette and intraplaquette nearest-neighbor bonds as order parameters. The dimer order parameter can be defined as

$$D = -\frac{2}{N} \sum_{\langle ij \rangle'} \langle S_i^z S_j^z \rangle, \tag{A1}$$

and the plaquette order parameter is defined as

$$P = -\frac{1}{N} \sum_{\langle ij \rangle} \langle S_i^z S_j^z \rangle. \tag{A2}$$

Here, $\langle ij \rangle'$ denotes the dimer bonds and $\langle ij \rangle$ denotes the intraplaquette bonds [79]. The parameter $N/2$ represents the number of the dimer bonds. We introduce minus signs in Eqs. (A1) and (A2) on account of the antiferromagnetic couplings. These two order parameters are also the hallmarks of first derivations of ground-state energy with respect to J and J' according to Hellmann–Feynman theorem.

Figure 12 shows the dimer order parameter D and the plaquette order parameter P versus the coupling ratios. As expected, the dimer order parameter D decreases and the plaquette order parameter P increases gradually as the coupling ratio J/J' is increased. Moreover, the first derivative of the plaquette order parameter P with respect to J/J' reaches a local maximum at the quantum critical point between the dimer phase and the Néel phase, which means a rapidly decreasing P when entering the dimer phase. Similarly, as shown in Fig. 12(b), the plaquette order parameter P dominates and the dimer order parameter D is reduced to near zero quickly in the PVBS phase.
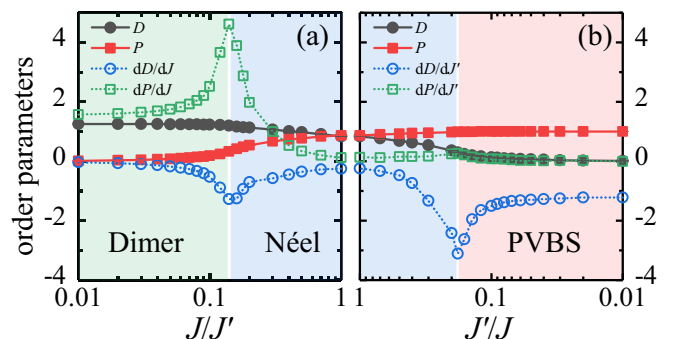

FIG. 12. The dimer order parameter D and the plaquette order parameter P are calculated by QMC simulations with $L = 8$. The phase boundaries deduced from the first derivatives of D and P with respect to the coupling ratios agree with our finite-size scaling results in the main text.
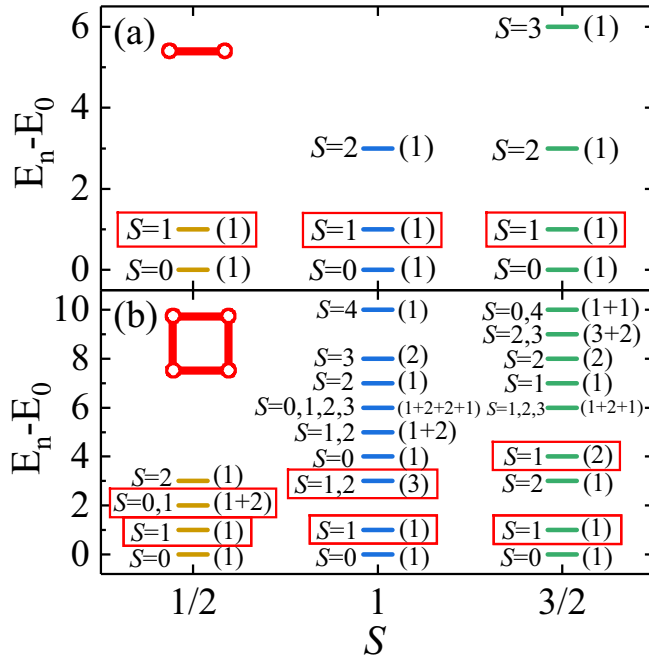
FIG. 13. Excitation spectra of (a) two-site and (b) four-site spin-S Heisenberg model in the $M_z = 0$ sector. We show the magnitude of the total spin angular momentum $\sqrt{S(S+1)}\hbar$ on the left of the energy levels and the degeneracy on the right of the energy levels. The red rectangle boxes represent the triplet excitations, which have nonzero weight in the $S^{zz}(\boldsymbol{q}, \omega) = \pi \sum_n |\langle n|S_{\boldsymbol{q}}^z|0\rangle|^2 \delta[\omega - (E_n - E_0)]$.

APPENDIX B: ISOLATED DIMER AND PLAQUETTE

The model we study has two limits with isolated dimer and plaquette. Here we show the excitation spectra of two-site and four-site Heisenberg models of spin-1/2,1 and 3/2 in the $M_z = 0$ sector using exact diagonalization, where M_z is the eigenvalue of the total spin component along the zth axis (see Fig. 13). In the dimer case, there is one triplet excitation above the singlet ground state, and the excitation energy is equal to $J' = 1$. In the plaquette case, there are two triplet excitations that contribute to the dynamic spin structure factors in Fig. 9 of the main text.

APPENDIX C: SEPARATION PROCESS BETWEEN THE LOW-ENERGY AND HIGH-ENERGY EXCITATIONS

In this Appendix, we further study the dynamical evolutions of the $S = 1/2$ and $S = 1$ antiferromagnetic Heisenberg model on the 1/5-depleted square lattice versus the coupling ratio J'/J. As shown in Fig. 14, the dynamic spin structure factor $S^{zz}(\boldsymbol{q}, \omega)$ is obtained from QMC calculations and stochastic analytic continuation with linear system size $M = 4$ of supercell and $\beta = 20$. We can find that the separation processes of the excitation spectra occur mainly between the coupling ratios $J'/J = 0.3$ and $J'/J = 0.5$. Similar to the $S = 3/2$ case in the main text, the separations between the low-energy and high-energy excitations do not always occur with the quantum phase transition synchronously, particularly in the $S = 1/2$ case.
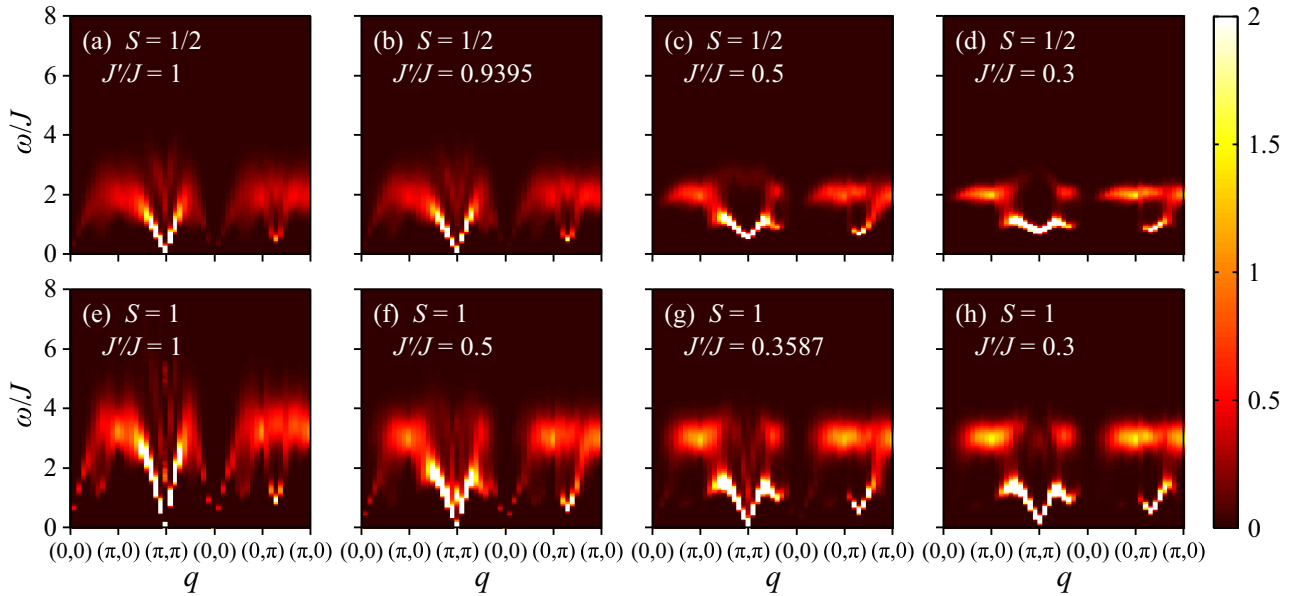

FIG. 14. The dynamic spin structure factor $S^{zz}(\boldsymbol{q}, \omega)$ of the $S = 1/2$ and $S = 1$ antiferromagnetic Heisenberg model on the 1/5-depleted square lattice with linear system size $M = 4$ of supercell and $\beta = 20$. (a), (e), and (f) are in the Néel phase, (b) and (g) are close to the quantum critical point J'_c, and (c), (d) and (h) are in the PVBS phase.

[1] H. Iwase, M. Isobe, Y. Ueda, and H. Yasuoka, J. Phys. Soc. Jpn. **65**, 2397 (1996).

[2] O. A. Starykh, M. E. Zhitomirsky, D. I. Khomskii, R. R. P. Singh, and K. Ueda, Phys. Rev. Lett. **77**, 2558 (1996).

[3] K. Ueda, H. Kontani, M. Sigrist, and P. A. Lee, Phys. Rev. Lett. **76**, 1932 (1996).

[4] M. Troyer, H. Kontani, and K. Ueda, Phys. Rev. Lett. **76**, 3822 (1996).

[5] S. R. White, Phys. Rev. Lett. **77**, 3633 (1996).

[6] J. Guo, S. Jin, G. Wang, S. Wang, K. Zhu, T. Zhou, M. He, and X. Chen, Phys. Rev. B **82**, 180520(R) (2010).

[7] A. F. Wang, J. J. Ying, Y. J. Yan, R. H. Liu, X. G. Luo, Z. Y. Li, X. F. Wang, M. Zhang, G. J. Ye, P. Cheng, Z. J. Xiang, and X. H. Chen, Phys. Rev. B **83**, 060512(R) (2011).

[8] A. Krzton-Maziopa, Z. Shermadini, E. Pomjakushina, V. Pomjakushin, M. Bendele, A. Amato, R. Khasanov, H. Luetkens, and K. Conder, J. Phys.: Condens. Matter **23**, 052203 (2011).

[9] H.-D. Wang, C.-H. Dong, Z.-J. Li, Q.-H. Mao, S.-S. Zhu, C.-M. Feng, H. Q. Yuan, and M.-H. Fang, Europhys. Lett. **93**, 47004 (2011).

[10] M.-H. Fang, H.-D. Wang, C.-H. Dong, Z.-J. Li, C.-M. Feng, J. Chen, and H. Q. Yuan, Europhys. Lett. **94**, 27009 (2011).

[11] X.-W. Yan, M. Gao, Z.-Y. Lu, and T. Xiang, Phys. Rev. B **83**, 233205 (2011).

[12] R. Yu, P. Goswami, and Q. Si, Phys. Rev. B **84**, 094451 (2011).

[13] W. Bao, Q.-Z. Huang, G.-F. Chen, D.-M. Wang, J.-B. He, and Y.-M. Qiu, Chin. Phys. Lett. **28**, 086104 (2011).

[14] M. Wang, C. Fang, D.-X. Yao, G. Tan, L. W. Harriger, Y. Song, T. Netherton, C. Zhang, M. Wang, M. B. Stone, W. Tian, J. Hu, and P. Dai, Nat. Commun. **2**, 580 (2011).

[15] Q. Luo, A. Nicholson, J. Riera, D.-X. Yao, A. Moreo, and E. Dagotto, Phys. Rev. B **84**, 140506(R) (2011).

[16] Y. Song, H. Cao, B. C. Chakoumakos, Y. Zhao, A. Wang, H. Lei, C. Petrovic, and R. J. Birgeneau, Phys. Rev. Lett. **122**, 087201 (2019).

[17] P. Dai, Rev. Mod. Phys. **87**, 855 (2015).

[18] R. Yu and Q. Si, Phys. Rev. Lett. **110**, 146402 (2013).

[19] Y.-T. Kang, C. Lu, F. Yang, and D.-X. Yao, Phys. Rev. B **99**, 184506 (2019).

[20] Y. Zhang, J. Lee, W.-L. Wang, and D.-X. Yao, Comput. Mater. Sci. **110**, 109 (2015).

[21] J. Li, S. Jin, F. Yang, and D.-X. Yao, Phys. Rev. B **102**, 174509 (2020).

[22] D. Schwandt, F. Alet, and S. Capponi, Phys. Rev. Lett. **103**, 170501 (2009).

[23] L. Weber, F. Parisen Toldin, and S. Wessel, Phys. Rev. B **98**, 140403(R) (2018).

[24] Z. Liu, J. Li, R.-Z. Huang, J. Li, Z. Yan, and D.-X. Yao, Phys. Rev. B **105**, 014418 (2022).

[25] A. Yamada, Phys. Rev. B **90**, 245139 (2014).

[26] Y. Yanagi and K. Ueda, Phys. Rev. B **90**, 085113 (2014).

[27] E. Khatami, R. R. P. Singh, W. E. Pickett, and R. T. Scalettar, Phys. Rev. Lett. **113**, 106402 (2014).

[28] A. Bao, H.-S. Tao, H.-D. Liu, X. Zhang, and W.-M. Liu, Sci. Rep. **4**, 6918 (2014).

[29] H.-Q. Wu, R.-Q. He, Z. Y. Meng, and Z.-Y. Lu, Phys. Rev. B **91**, 125128 (2015).

[30] L. Zhang and F. Wang, Phys. Rev. Lett. **118**, 087201 (2017).

[31] I. Affleck, T. Kennedy, E. H. Lieb, and H. Tasaki, Phys. Rev. Lett. **59**, 799 (1987).

[32] I. Affleck, T. Kennedy, E. H. Lieb, and H. Tasaki, Commun. Math. Phys. **115**, 477 (1988).

[33] C.-M. Jian, Z. Bi, and C. Xu, Phys. Rev. B **97**, 054412 (2018).

[34] D. Gross and J. Eisert, Phys. Rev. Lett. **98**, 220503 (2007).

[35] G. K. Brennen and A. Miyake, Phys. Rev. Lett. **101**, 010502 (2008).

[36] X. Chen, R. Duan, Z. Ji, and B. Zeng, Phys. Rev. Lett. **105**, 020502 (2010).

[37] T.-C. Wei, I. Affleck, and R. Raussendorf, Phys. Rev. Lett. **106**, 070501 (2011).

[38] N. Pomata and T.-C. Wei, Phys. Rev. Lett. **124**, 177203 (2020).

[39] T.-C. Wei and R. Raussendorf, Phys. Rev. A **92**, 012310 (2015).

[40] F. Verstraete and J. I. Cirac, Phys. Rev. A **70**, 060302(R) (2004).

[41] T.-C. Wei, Phys. Rev. A **88**, 062307 (2013).

[42] H. J. Briegel, D. E. Browne, W. Dür, R. Raussendorf, and M. Van den Nest, Nat. Phys. **5**, 19 (2009).

[43] J. Lou, S. Tanaka, H. Katsura, and N. Kawashima, Phys. Rev. B **84**, 245128 (2011).

[44] C.-Y. Huang, X. Chen, and F.-L. Lin, Phys. Rev. B **88**, 205124 (2013).

[45] Y.-Z. You, Z. Bi, A. Rasmussen, K. Slagle, and C. Xu, Phys. Rev. Lett. **112**, 247202 (2014).

[46] K. Wierschem and P. Sengupta, Phys. Rev. B **90**, 115157 (2014).

[47] K. Wierschem and K. S. D. Beach, Phys. Rev. B **93**, 245141 (2016).

[48] A. S. Darmawan, G. K. Brennen, and S. D. Bartlett, New J. Phys. **14**, 013023 (2012).

[49] C.-Y. Huang, M. A. Wagner, and T.-C. Wei, Phys. Rev. B **94**, 165130 (2016).

[50] J. Kim, J. Chaloupka, Y. Singh, J. W. Kim, B. J. Kim, D. Casa, A. Said, X. Huang, and T. Gog, Phys. Rev. X **10**, 021034 (2020).

[51] J. Chaloupka and G. Khaliullin, Phys. Rev. B **92**, 024413 (2015).

[52] A. W. Sandvik, AIP Conf. Proc. **1297**, 135 (2010).

[53] A. W. Sandvik, Phys. Rev. B **59**, R14157 (1999).

[54] O. F. Syljuåsen and A. W. Sandvik, Phys. Rev. E **66**, 046701 (2002).

[55] S. Bergkvist, P. Henelius, and A. Rosengren, Phys. Rev. B **66**, 134407 (2002).

[56] M. Troyer, M. Imada, and K. Ueda, J. Phys. Soc. Jpn. **66**, 2957 (1997).

[57] Y.-C. Wang, Y. Qi, S. Chen, and Z. Y. Meng, Phys. Rev. B **96**, 115160 (2017).

[58] A. F. Albuquerque, C. J. Hamer, and J. Oitmaa, Phys. Rev. B **79**, 054412 (2009).

[59] M. Campostrini, M. Hasenbusch, A. Pelissetto, P. Rossi, and E. Vicari, Phys. Rev. B **65**, 144520 (2002).

[60] L. Wang, K. S. D. Beach, and A. W. Sandvik, Phys. Rev. B **73**, 014431 (2006).

[61] X. Ran, N. Ma, and D.-X. Yao, Phys. Rev. B **99**, 174434 (2019).

[62] N. Ma, P. Weinberg, H. Shao, W. Guo, D.-X. Yao, and A. W. Sandvik, Phys. Rev. Lett. **121**, 117202 (2018).

[63] F.-J. Jiang, Phys. Rev. B **85**, 014414 (2012).

[64] S. Wenzel, L. Bogacz, and W. Janke, Phys. Rev. Lett. **101**, 127202 (2008).

[65] Z. Yan, Z. Zhou, O. F. Syljuåsen, J. Zhang, T. Yuan, J. Lou, and Y. Chen, Phys. Rev. B **103**, 094421 (2021).

[66] C. Ding, L. Zhang, and W. Guo, Phys. Rev. Lett. **120**, 235701 (2018).

[67] E. Manousakis, Rev. Mod. Phys. **63**, 1 (1991).

[68] A. W. Sandvik, Phys. Rev. Lett. **98**, 227202 (2007).

[69] R. R. P. Singh, M. P. Gelfand, and D. A. Huse, Phys. Rev. Lett. **61**, 2484 (1988).

[70] M. Matsumoto, C. Yasuda, S. Todo, and H. Takayama, Phys. Rev. B **65**, 014407 (2001).

[71] Y. Xu, Z. Xiong, H.-Q. Wu, and D.-X. Yao, Phys. Rev. B **99**, 085112 (2019).

[72] N. Ma, G.-Y. Sun, Y.-Z. You, C. Xu, A. Vishwanath, A. W. Sandvik, and Z. Y. Meng, Phys. Rev. B **98**, 174421 (2018).

[73] N. Ma, Y.-Z. You, and Z. Y. Meng, Phys. Rev. Lett. **122**, 175701 (2019).

[74] C. Hickey, M. Gohlke, C. Berke, and S. Trebst, Phys. Rev. B **103**, 064417 (2021).

[75] H. Shao and A. W. Sandvik, arXiv:2202.09870.

[76] M. Mourigal, M. Enderle, A. Klöpperpieper, J.-S. Caux, A. Stunault, and H. M. Rønnow, Nat. Phys. **9**, 435 (2013).

[77] A. Maity, Y. Iqbal, and S. Mandal, Phys. Rev. B **102**, 224404 (2020).

[78] D. Poilblanc, N. Schuch, and J. I. Cirac, Phys. Rev. B **88**, 144414 (2013).

[79] H. H. Zhao, C. Xu, Q. N. Chen, Z. C. Wei, M. P. Qin, G. M. Zhang, and T. Xiang, Phys. Rev. B **85**, 134416 (2012).